Soft Matter

Accepted Manuscript

This is an *Accepted Manuscript*, which has been through the Royal Society of Chemistry peer review process and has been accepted for publication.

Accepted Manuscripts are published online shortly after acceptance, before technical editing, formatting and proof reading. Using this free service, authors can make their results available to the community, in citable form, before we publish the edited article. We will replace this *Accepted Manuscript* with the edited and formatted *Advance Article* as soon as it is available.

You can find more information about *Accepted Manuscripts* in the Information for Authors.

Please note that technical editing may introduce minor changes to the text and/or graphics, which may alter content. The journal's standard Terms & Conditions and the Ethical guidelines still apply. In no event shall the Royal Society of Chemistry be held responsible for any errors or omissions in this *Accepted Manuscript* or any consequences arising from the use of any information it contains.

ROYAL SOCIETY OF CHEMISTRY

www.rsc.org/softmatter

Controlling mechanisms in directional growth of aggregated archaeal cells

Viktor Milkevych*, Damien J. Batstone**

* Department of Engineering, Aarhus University, Hangøvej 2, 8200 Aarhus N, Denmark
** Advanced Water Management Centre, The University of Queensland, Saint Lucia, Gehrmann Building (60), QLD 4072, Australia

ABSTRACT

Members of the family *Methanosarcinaceae* are important archaeal representatives due to their broad functionality, ubiquitous presence, and functionality in harsh environments. A key characteristic is their multicellular (packet) morphology represented by aggregates of spatially confined cells. This morphology is driven by directed growth of cells in confinement with sequential variation in growth direction. To further understand why spatially confined *Methanosarcina* cells (and in general, confined prokaryotes) change their direction of growth during consecutive growth-division stages, and how a particular cell senses its wall topology and responds to changes on it a theoretical model for stress dependent growth of aggregated archaeal cells was developed. The model utilizes a confined elastic shell representation of aggregated archaeal cell and is derived based on a work-energy principle. The growth law takes into account the fine structure of archaeal cell wall, polymeric nature of methanochondroitin layer, molecular-biochemical processes and is based on thermodynamic laws. The developed model has been applied to three typical configurations of aggregated cell in 3D. The developed model predicted a geometry response with delayed growth of aggregated archaeal cells explained from mechanistic principles, as well as continuous changes in direction of growth during the consecutive growth-division stages. This means that cell wall topology sensing and growth anisotropy can be predicted using simple cellular mechanisms without the need for dedicated cellular machinery.

1. Introduction

Microbial cells often form aggregates (Fig. 1) where they: a) remain attached after division; b) become confined by neighbor cells; and c) continuously increase their confinement during further growth within the aggregate [1-10]. Multicellular formations are widely found in different engineered and natural environments, and their characteristics propagate to larger multicellular structures such as biofilms.

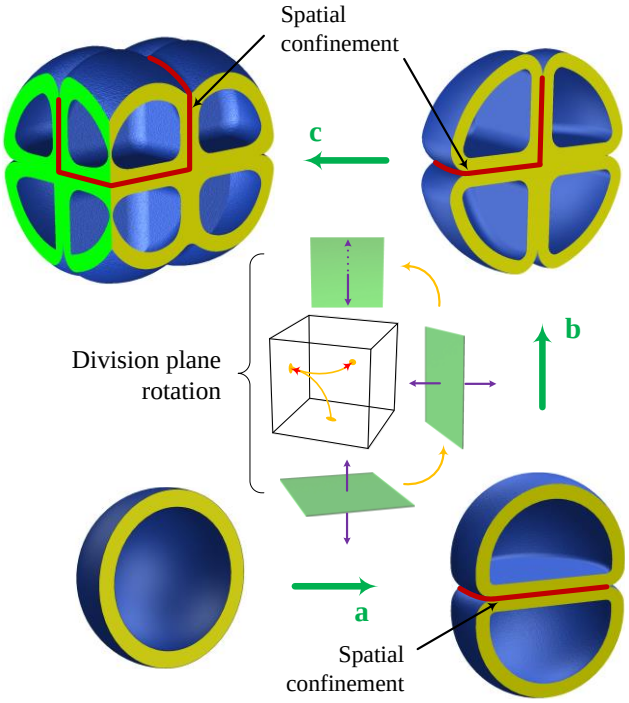

Fig 1. Successive stages of aggregate formation in *Methanosarcina*. Green arrows indicate the direction of aggregate evolution. (a) - transition from the initial spatially unconfined spherical cell to two-cells aggregate where the cells remains attached after the division and became spatially confined. The red line indicates the border of confinement region. (b) - transition from two-cells aggregate to four-cells aggregate, and (c) – to eight-cells aggregate. The consecutive change in shape of particular aggregated cell as well as its confinement state during transition from (a) to (c) is observed. Blue arrows indicate the direction of growth and division. The orange arrows point out on division plane rotation in transition stages from (a) to (c) during aggregate evolution. The green plane visualizes division planes and their orientations.

Particularly within the Archaea, which have received less biophysical analysis than Bacteria or Eukaryotes, *Methanosarcinaceae* of the order *Methanosarcinales* [1, 11] are important aggregate forming microbes. They are strictly anaerobic methane-producing microbes, and obtain energy from methanogenesis by catalyzing the terminal step of organic matter degradation process in anoxic environments [1, 11, 12]. They have a diverse substrate capacity, and are the only Archaea capable of mediating a wide range of primary substrates such as acetate, formate, hydrogen and methanol [13]. The aggregate type of multicellular organizational structure is important, since it potentially influences mass transfer and interspecies relationships, particularly those that rely on short interspecies distances such as syntrophic organic acid oxidation [14]. The aggregate structure should theoretically disadvantage *Methanosarcinaceae* from a substrate transfer point of view, but they are widespread in engineered environments, particularly where conditions are disadvantageous to other competing organisms such as *Methanosaetaceae* [15]. It is unknown as to whether the aggregate

structure is related to the morphological capabilities and environmental tolerance of *Methanosarcina*.

Methanosarcina, [1, 2] as well as some other prokaryotes (like spheroidal *Escherichia coli* [3, 4], *Sarcinae* [5, 6], *Staphylococcus aureus* [7, 9, 10]) are subject to growth anisotropy due to the post division attachment of sibling cells and their preserved confinement, Fig. 1. This leads to variations in directional cell wall growth and division plane orientation. Such variations follow consecutive growth-division stages of the cells within the aggregate and depend on the state of confinement. Strongly confined cells within the aggregate possess substantially different shapes from unconfined cells and normally are subject to orthogonal variations in directional cell wall growth and division plane orientation [2, 7].

There are two important questions that essential to understanding divers of morphology: (a) why do spatially confined *Methanosarcina* cells (and in general, confined prokaryotes) change their direction of growth during consecutive growth-division stages? and (b) how does a particular cell sense its wall topology and respond to changes on it?

While these questions have not been previously addressed, there has been substantial work on the growth of spatially confined eukaryotic cells [16-21], largely in relation to tissue growth.

Cell-level geometric control of eukaryotic cells was observed in [19]. Considering human and bovine capillary endothelial cells growth, the authors discovered that the cell shape was able to govern whether individual cells grow or die by using micropatterned substrates that contained extracellular matrix-coated adhesive islands of decreasing size to progressively restrict cell extension. Further, in [17] was shown that the local tissue growth rate is strongly influenced by the three-dimensional confinement. This enabled a conclusion that cells within the tissue were able to sense and respond to substantially larger radii of curvature than the cell size. The theoretical explanation of observed effects of tissue growth in confined space was done [16] by application of a theoretical framework previously developed [22, 23]. This resulted in a volumetric growth rate term consistent with the laws of thermodynamics and observed results in the case of tissue growth within the circular pore. Mechanical stress is produced during the tissue growth and it has the strong contribution on the growth rate and direction itself.

The response in eukaryotic cells to spatial confinement through stress dependent growth and a cell sensing mechanism is probably based on microtubule orientation inside the cell [20, 21]. Due to the structural and functional differences between the eukaryotes and prokaryotes this mechanism is not applicable to Archaea, especially in case of sensing mechanism (since there are no microtubules in Archaea).

In order to address the problem of growth of prokaryotic cell within the aggregated (spatially confined) state, we have applied theoretical analysis based on a mathematical model for growth of confined prokaryotes, with a focus on Archaea, and particular application to *Methanosarcina*.

2. Model

2.1. Cell mechanical model

A number of basic simplifying assumptions enable translation of the biological system to a mechanical system. However, the necessary key assumption used in this study is that a cell can be represented as a thin elastic shell. This assumption is extensively applied approach in modeling

microbial cells [24-28], but we justify this further here for the particular case of aggregated archaeal cells.

2.1.1. Basic assumptions

In the particular case of microbial cells, fine structural properties have to be taken into account since these determine diversity in morphotypes and allow correct translation to a formal modeling object. The fine structure of *Methanosarcina* cell wall is shown at Fig. 2. The cell wall consists of three major components (see the Supplementary Materials for more details): cytoplasmic membrane, surface layer proteins (S-layer) and heteropolysaccharide layer (matrix) [29]. The cytoplasmic membrane appears in bilayer structure of hydroxylated diether lipids (3-hydroxyarchaeols) [30, 31], with a thickness of bilayer $4.5\,\text{nm}$ [29]. The S-layer is the outmost boundary of the cell envelop and can be considered as a protective, porous barrier [32], with an average thickness of the layer $10-12\ \text{nm}$ [2, 33]. The third component, the heteropolysaccharide matrix, has a thickness of $20-200\,\text{nm}$ and is composed of fibrillar polymer methanochondroitin, which possess a molecular mass of about $10\,\text{kDa}$ [34]. The matrix appears as loosely packed fibrils initially polymerized parallel to the S-layer [35].

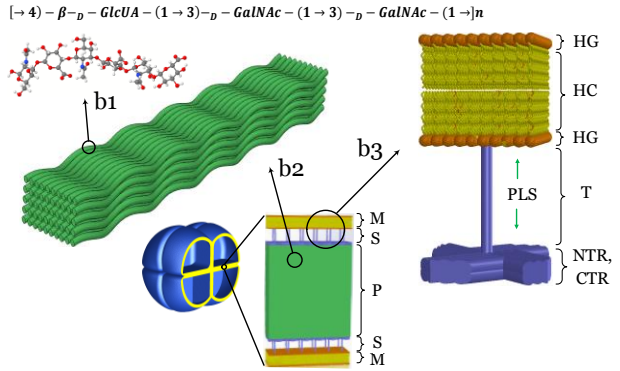

Fig. 2. Fine structure of *Methanosarcina* cell wall. Arrow **b1** identifies molecular structure of polymeric filament, according to [36]. GalNAc is N-acetylgalactosamines; GlcUA is glucuronic acid. Arrow **b2** identifies polymeric layer of fibrillar methanochondroitin. Arrow **b3** identifies parts of the cytoplasmic membrane and S-layer: HG is a headgroup and HC is hydrophobic core of hydroxylated diether lipid; NTR and CTR are C-terminal dimers and T is a tether region of S-layer proteins; PLS is a periplasmic-like space. M is a cytoplasmic membrane; S is a S-layer; P is a methanochondroitin layer (current picture shows the doubled methanochondroitin layer).

This representation allows the following additional assumptions:

1) Among the coupling "bilayer cytoplasmic membrane – S-layer", mostly the S-layer contributes to structural rigidity [32] but is thin compared to the matrix (the ratio $\sim 0.10-0.17$) and is not able to simulate behavior under confinement. Confined cells with significantly depleted methanochondroitin layer gain a pure spherical shape, became fragile and are predicted to lyse [1].

Hence, it is reasonable to neglect the properties related to structural rigidity of this coupling due to its insignificant impact on cell structural rigidity compared to methanochondroitin layer.

2) We consider the methanochondroitin matrix layer as an isotropic network of entangled semiflexible polymers.

3) In general, the cell wall responds to mechanical loading as a visco-elastic material [37], but with three different time scales: for growth (τ_G), viscous (τ_V) and elastic (τ_E) responses, $\tau_G \gg \tau_V > \tau_E$. As such the visco-elastic part can be simulated as a single fast elastic process with new time scale τ_{E^*} which combine τ_V and τ_E, with $\tau_G \gg \tau_{E^*}$. These two time-scales are decoupled and represented as a set of small quasistatic successive incremental growth steps with unloaded configuration followed by elastic relaxation at each incremental step [38, 39].

2.1.2. Mechanical equilibrium of confined elastic shell

Here, the aggregated archaeal cell is represented as a confined thin elastic shell (the detailed justification of such representation is given in the Supplementary Materials). The geometrical details of modeled cell are shown in Fig. 3.

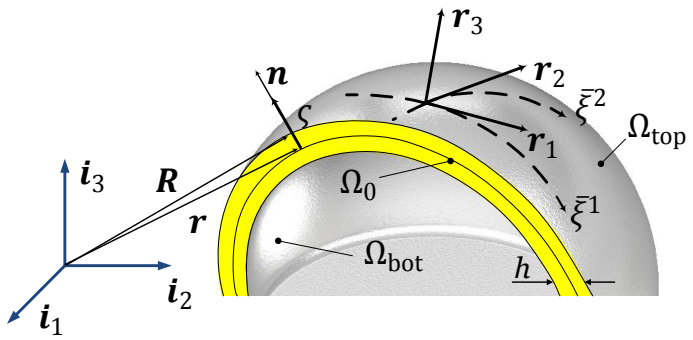

Fig. 3. Geometrical model of the cell. Ω_0 is smooth surface inside the cell wall; $\Omega_{\text{top, bot}}$ is top and bottom surfaces of the cell wall; ς is coordinate counted along the direction perpendicular to Ω_0; $\boldsymbol{R}$ is radius vector of any point in the cell; $\boldsymbol{r}$ is parametrization of Ω_0 with unit-normal field $\boldsymbol{n}$; $\bar{\xi}^\alpha$ $(\alpha = 1,2)$ is curvilinear coordinate system in reference configuration; i_β, $\beta = 1,2,3$ is global orthogonal coordinate system; r_β is local orthogonal coordinate system; h is cell wall thickness.

The equilibrium equations for considering confined shell may be expressed in the following compact form:

$$\operatorname{div}(\boldsymbol{T}) = 0, \quad (1a)$$

$$\operatorname{div}(\boldsymbol{M}) + \boldsymbol{T}_\times = 0, \quad (1b)$$

where $\boldsymbol{T}$ is stress tensor; $\boldsymbol{T}_{\times}$ is vector invariant of $\boldsymbol{T}$, $\boldsymbol{T}_{\times} \equiv \boldsymbol{r}_{\alpha} \times \boldsymbol{T}^{\alpha}$; $\boldsymbol{M}$ is internal moment tensor; $\mathrm{div}(*) = \boldsymbol{r}^{\alpha} \dfrac{\partial}{\partial \xi^{\alpha}}$ represents the surface divergence.

The boundary conditions are the following:

1) The shell is loaded by the turgor pressure $\boldsymbol{P}$ on the bottom surface of the cell wall Ω_{bot}, the boundary condition is represented by $\boldsymbol{T}$ in the normal direction $\boldsymbol{n}$ of Ω_{bot} (Fig. 3):

$$\boldsymbol{T} \cdot \boldsymbol{n} = -p\boldsymbol{n}|_{\Omega_{\mathrm{bot}}}. \quad (2)$$

2) Consider the confined part of the cell top surface $\Omega_{\mathrm{conf}} \subset \Omega_{\mathrm{top}}$ (Fig. 3). It is the surface directly connected to the neighbor cell and shares with it doubled methanochondroitin layer (restricted to Ω_{conf}). We model cell-cell cohesiveness on Ω_{conf} using cohesive springs with a linear cohesive force law:

$$A \cdot \mathrm{div}(\boldsymbol{T}) = \vartheta \boldsymbol{u}|_{\Omega_{\mathrm{conf}}}, \quad (3)$$

where A is the area of Ω_{conf}, ϑ is the spring constant, $\boldsymbol{u}$ is the displacement field. This models cell-cell interaction and retains cell shape integrity (i.e., prevents cell deformation) in response to directional forces.

3) The remaining part of the boundary $\Omega_{\mathrm{free}} = \Omega_{\mathrm{top}} \setminus \Omega_{\mathrm{conf}}$ is free of loading:

$$\boldsymbol{T} \cdot \boldsymbol{n} = 0|_{\Omega_{\mathrm{free}}}. \quad (4)$$

2.2. Cell growth model

A model for growth of confined archaeal cells is developed based on work-energy principle, introduced in [39] and further elaborated in [22, 23, 40]. This includes the fine cell wall structure, molecular-biochemical processes as well as application of the above assumptions to derive growth equations consistent with thermodynamic principles.

2.2.1. Structural model of polymeric network in a growing cell wall

As described in section 2.1, the cell wall material assumed to be a dense polymeric network, where each polymeric filament exists in a confined environment formed by other filaments (Fig. 4). Single polymer confinement can be modeled as a tube with characteristic diameter d, and a polymer dynamics can be described as an reptation motion [41]. During the cell wall growth each polymer of the methanochondroitin matrix is subject to (Fig. 4): a) changes in its conformation, and hence associated constrained tube conformation; b) changes in constrained tube diameter and; c) lateral movement within a constrained tube (reptation) induced by external (in relation to the tube) loading.

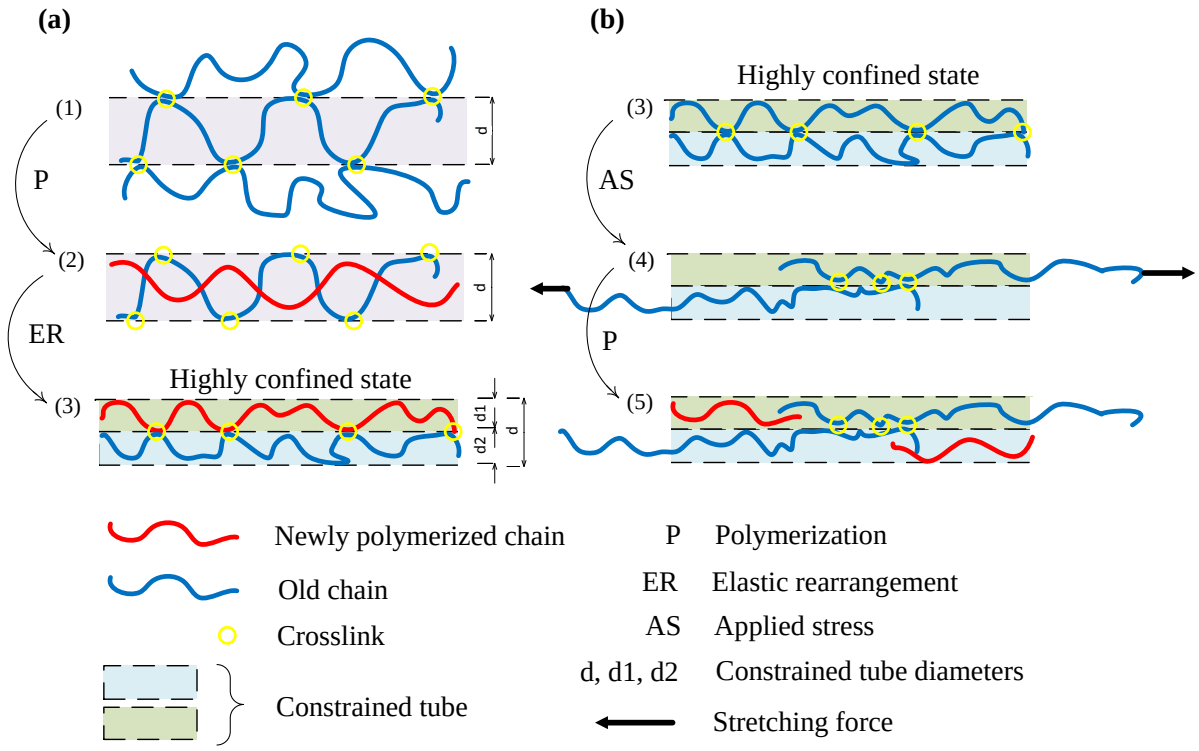

Fig. 4. Structural organization of polymeric network in a growing cell wall. **(a)** Visualization of free polymerization type of growth. (1) The initial sparse network, where the central filament is in a constrained tube. (2) A new chain is polymerized inside the constrained tube, which leads to (3) elastic rearrangement of polymers inside the tube which induce transformation of initial constrained tube to two tubes with smaller diameters, *d1* and *d2*, and overall increase in density. Such processes (1)-(3) repeat until a confined chains free energy reach the maximal values which corresponds to highly confined state and a very dense polymeric network. **(b)** Visualization of stress induced type of cell wall growth. It is possible if at the stage (3) the external force load is applied which induce a reptation motion inside a constrained tube, (4). This changes the constrained tube diameter and the free energy of confined polymers, otherwise creates the space for new filaments polymerization, (5).

Overall, the cell wall material can be characterized by the chemical potential μ_{conf} which is a function of polymer concentration and confinement strength characterized by confinement size d: $\mu_{\text{conf}} = \mu_{\text{conf}}(\phi, d)$. Furthermore, μ_{conf} can be represented as an additive decomposition [42] $\mu_{\text{conf}} = \mu_{\text{conf}}(\phi) + \mu_{\text{conf}}(d)$, where $\mu_{\text{conf}}(\phi)$ accounts for the concentration dependence of unconfined methanochondroitin solution and $\mu_{\text{conf}}(d)$ accounts for the confinement dependence of isolated methanochondroitin filament.

2.2.2. Cell wall material deformation

Consider the deformation of cell wall material (represented here according to the structural model, Fig. 4) within arbitrary volume V^0 of cell $\Theta \in \mathbb{R}^3$. Two homogeneous domains (in terms of deformation gradient) V^{II} and V^{III} exist within V^0 such that $V^{II} + V^{III} = V^I \subset V^0$ (Fig. 5), where V^I is not necessarily homogeneous. The volume fraction of the domain within V^{II} is given as $\varphi^* = V^{II}/V^I$ and for V^{III} is $(1-\varphi^*)$.

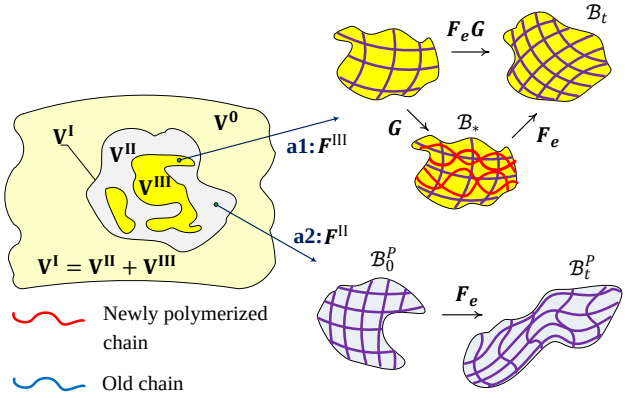

Fig. 5. Homogeneous domains of cell wall material and corresponding deformation gradients. V^I, V^{II}, V^{III} are the volumes enclosed the different domains within an arbitrary part V^0 of a cell wall material. Arrows **a1** and **a2** point out on different types of deformations which are carried out within to different homogeneous domains associated with V^{II} and V^{III}. The deformation defined by $\boldsymbol{F}^{II}$ describes the mapping of initially stressed reference state $\mathcal{B}_0^P$ to another relaxed state $\mathcal{B}_t^P$ where the condition of displacement field compatibility is always satisfied; it is a pure elastic deformation with no growth associated. The deformation defined by $\boldsymbol{F}^{III}$ describes the mapping of reference zero-stress state $\mathcal{B}_0$ to a new stressed state $\mathcal{B}_t$ which is characterized by growth induced residual stress. Transition from $\mathcal{B}_0$ to $\mathcal{B}_t$ is realized through the locally stress-free transient state $\mathcal{B}_*$ by the mapping $\boldsymbol{G}$, which though may not be compatible, and next, by the mapping $\boldsymbol{F_e}$, which make the deformation compatible. $\boldsymbol{F}^{III}$ involves a new material polymerization inside the domain and further elastic relaxation of all polymeric material to a new internally stressed polymeric network.

For the arbitrary domain enclosed by V^I the work done by the internal stresses forces may be expressed as:

$$\int \delta R^I dV^I = \int \left(\varphi \frac{\partial \sigma_{ik}}{\partial x_k} \delta u_i + (1-\varphi) \frac{\partial \sigma_{jk}}{\partial x_k} \delta u_j \right) dV^I, \quad (5)$$

where $\boldsymbol{u}$ is deformation vector which is subject to small $\delta \boldsymbol{u}$; $f_i = \partial \sigma_{ik} / \partial x_k$, $f_j = \partial \sigma_{jk} / \partial x_k$ are internal stresses forces; δu_i, δu_j are deformation vectors due to forces f_i and f_j respectively; φ is a scalar-valued function defined on the interval $[0,1]$.

From (5) the work done δR^I can be derived as

$$\delta R^{I} = -\varphi \boldsymbol{P} : \delta \boldsymbol{F}^{III} - (1-\varphi)\boldsymbol{P} : \delta \boldsymbol{F}^{II}, \quad (6)$$

where $\boldsymbol{P}$ is the 1st Piola-Kirchhoff stress tensor; $\boldsymbol{F}^{II}$ and $\boldsymbol{F}^{III}$ are the deformation gradients which are relates to deformation vectors δu_i, δu_j respectively and are associated with specific homogeneous domains (Fig. 5).

The deformation defined by $\boldsymbol{F}^{II}$ describes the mapping of initially stressed reference state $\mathcal{B}_0^P$ to another relaxed state $\mathcal{B}_t^P$ where the condition of displacement field compatibility is always satisfied. The loading of the reference state $\mathcal{B}_0^P$ can be due to 1) the external loading of a cell wall by turgor pressure and/or adhered neighboring cells, and 2) the internal loading (within the volume V^I) by neighboring growth performing domain (V^{III} in Fig. 5) which generates the residual stress during the growth. $\boldsymbol{F}^{II}$ is a pure elastic deformation and there is no new material polymerization (simply no growth) carried out in the domain enclosed by V^{II}.

The deformation defined by $\boldsymbol{F}^{III}$ describes the mapping of reference zero-stress state $\mathcal{B}_0$ to a new stressed state $\mathcal{B}_t$ which is characterized by growth induced residual stress. Transition from $\mathcal{B}_0$ to $\mathcal{B}_t$ is realized through the locally stress-free transient state $\mathcal{B}_*$ by the mapping $\boldsymbol{G}: \mathcal{B}_0 \to \mathcal{B}_*$ (Fig. 5) which though may not be compatible. $\boldsymbol{F}^{III}$ involves a new material polymerization inside the domain and further elastic relaxation of all polymeric material to a new internally stressed polymeric network (Fig. 4).

Following by [43], we represent the deformation gradient $\boldsymbol{F}^{III}$ as an multiplicative decomposition consisting of pure elastic deformation gradient $\boldsymbol{F}_e$ and the growth deformation gradient $\boldsymbol{G}$. By taking this into account, $\boldsymbol{F}^{II}$ and $\boldsymbol{F}^{III}$ will have the following representation:

$$\boldsymbol{F}^{III} = \boldsymbol{F}_e \boldsymbol{G}, \quad (7a)$$
$$\boldsymbol{F}^{II} = \boldsymbol{F}_e \boldsymbol{I}, \quad (7b)$$

where $\boldsymbol{I}$ is the identity tensor. From (7) the first term in right hand side of (6) can be understood as a work done by pure growth forces, which are caused by monosaccharaide polymerization (depolymerization) with further elastic material response; the second term can be understood as a work done by pure elastic response of material under the loading without any additional forces induced by growth. Since the stress tensor $\boldsymbol{P}$ is defined in V^I and is a volume averaged for an inhomogeneous domain, the contribution of different homogeneous domains (associated with V^{II} and V^{III}) in a total work done in V^I is defined by the function φ which can be represented as $\varphi = \varphi(\varphi^*)$. This function takes the role of partitioning mechanism which splits the total amount of work for two parts, the work done by pure growth R_G and the work done by pure mechanical response R_E: $R^I = R_G + R_E$.

2.2.3. Growth eigenstrain rate

The growth eigenstrain rate can be expressed as follows (see the complete derivation in Supplementary Materials)

$$\dot{\boldsymbol{g}} = \chi(\phi)\left[\varphi \boldsymbol{F}^{\boldsymbol{T}} \boldsymbol{P} - \rho \Psi \boldsymbol{E}_0 - \rho \mu_{\text{conf}} \boldsymbol{E}_{\boldsymbol{p}}\right], \quad (8)$$

where $\dot{\boldsymbol{g}}$ is the growth eigenstrain rate, the upper dot corresponds to the material time derivative; $\chi(\phi)$ is a scalar function of cell wall polymers concentration ϕ; φ is the partition function which splits the total amount of work for two parts, the work done by pure growth R_G and the work done by pure mechanical response R_E (section 2.2.2); $\boldsymbol{F}$ is deformation gradient; $\boldsymbol{P}$ is the 1st Piola-Kirchhoff stress tensor; ρ is the cell wall material density in actual configuration; Ψ is the free energy of confined elastic shell; $\boldsymbol{E}_0$ is the tensor that describe the material absorption rate anisotropy; μ_{conf} is a chemical potential which characterize the cell wall material (see section 2.2.1 and the Supplementary Materials for details in μ_{conf} definition); $\boldsymbol{E}_{\boldsymbol{p}}$ is the tensor that describe the anisotropy in monosaccharaides polymerization rate inside the cell wall.

2.2.4. Constitutive equation for the function φ

During growth, the cell wall is subject to bending and stretching. Hence, the total free energy of confined elastic shell Θ is given as [44]: $\Psi_\Theta = \int(\Psi_{\text{bnd}} + \Psi_{\text{str}})d\text{f}$, where $d\text{f}$ is a surface element; Ψ_{bnd} is a bending energy; Ψ_{str} is a stretching energy. Bending exerts compression of the material of shell Θ, that leads to increase of μ_{conf}, so the decrease in polymerization rate and hence decrease in growth rate can be observed within the bending region. Stretching above the certain energy barrier can change the cell wall structure in terms of rearrangement of entangled polymer network (Fig. 4), so the decrease of μ_{conf} can be observed, and increase in growth rate takes place in stretching region. From these considerations the partition function, which quantitatively defines the partial contribution of internal stress forces to growth (as it can be seen from Eq. 8), can be expressed as $\varphi \simeq \varphi_{\text{mech}}$, $\varphi_{\text{mech}} = \varphi_{\text{mech}}(\Psi_{\text{bnd}}, \Psi_{\text{str}})$ and now reads:

$$\varphi_{\text{mech}} = \Psi_{\text{str}}(\Psi_{\text{bnd}} + \Psi_{\text{str}})^{-1}. \quad (9)$$

2.3. Computational details

Eq. (8) can be reformulated it in a simpler form:

$$\dot{\boldsymbol{g}} = \chi(\phi)\left[\varphi_{\text{mech}}\boldsymbol{\sigma} - \varphi_{\text{conf}}\boldsymbol{E}_{\boldsymbol{p}}\right], \quad (10)$$

where $\boldsymbol{\sigma}$ is a Cauchy stress tensor; $\varphi_{\text{conf}} = \rho\varsigma\Psi + \rho\mu_{\text{conf}}$, $\Psi = \Psi_{\text{bnd}} + \Psi_{\text{str}}$, $\boldsymbol{E}_0 \simeq \varsigma\boldsymbol{E}_{\boldsymbol{p}}$, here ς is a proportional coefficient. The term $\varphi_{\text{conf}}\boldsymbol{E}_{\boldsymbol{p}}$ in (10) relates to reduction in growth rate because of increase in confinement free energy due to high polymerization intensity.

Additionally, the scalar-valued function of growth potential can be calculated as a supplemental output (in addition to 3D geometry dynamics):

$$\mu_G = \chi\varphi_{\text{mech}}\sigma_{\text{vm}}, \quad (11)$$

where μ_G is the cell wall growth potential and σ_{vm} is von Mises stress. Cell wall growth potential is used to represent complex stress state of archaeal cell wall during growth and relates to simplified growth model $\dot{\boldsymbol{r}} \sim \mathrm{grad}(\mu_G)$.

The overall problem is formulated as quasistatic successive incremental growth (see the section 2.1). For each incremental time step problem solution consists of three major stages: 1) solving the equilibrium problem, Eq. (1)-(4), for an aggregated cell (Fig. 6), which gives the stress field for confined shell; then 2) solving Eq. (10) which gives the growth induced strain field and the necessary stretches ratios, in addition to this the growth potential, Eq. (11), is also calculated which gives visualizing data to be mapped on 3D geometry; and 3) performing the necessary cell geometry changes using calculated stretch ratios. Each incremental time step is repeating until the cells volume is doubled. After the simulation the growth time is normalized.

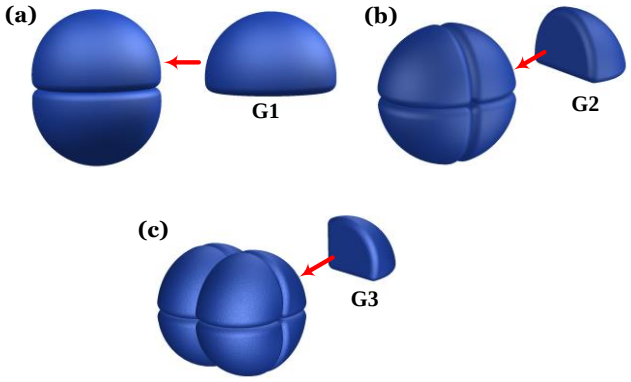

Fig. 6. Representative conformations of confined *Methanosarcina* cells. **(**a)-(c): the basic types of *Methanosarcina* multicellular formations and particular representative conformations of cells (the top right part of each picture) which were used as modeled objects. Red arrows indicate the placement of confined cell within aggregate.

Three different geometrical representations of the cells have been used during simulations, Fig. 6. These geometrical representations correspond to representative conformation of cells which are configurations likely to be observed (see the Supplementary Materials for the formal definition).

The solution scheme follows the following steps. First, the problem is solved by applying a finite element method (using COMSOL Multiphysics 4.3a, COMSOL, Inc., Burlington, MA). At the next stage Eq. (10) is integrated applying finite differencing which gives the necessary geometry changes (growth) provided through a self-writing code using MatLab R2010b, The MathWorks, Inc. Some other 3D geometry operations (mainly related to the transformations of point cloud object to the closed surface in 3D) were performed in MeshLab v. 1.3.2. A detailed flow scheme of calculation process is shown in Fig. S4.

The following parameters were applied for numerical calculations. Assuming Poisson ratio $\nu = 0.4$ and spring constant in (3) $\vartheta = 5 \cdot 10^{-3}\ \mathrm{nPa \cdot nm^{-1}}$. According to [2] and considered earlier assumptions, accepted cell wall thickness is $h = 0.06 \cdot 10^{-6}\ \mathrm{m}$. There are no mechanical properties have been reported for *Methanosarcina* species, thus here we use our data (unpublished data, based on atomic force microscopy measurements of *Methanosarcina barkeri*) in relation to the mechanical

properties and the turgor pressure for *Methanosarcina*. The parameters were used in calculations are the following: the Young's modulus $E = 78$ MPa and the turgor pressure $P = 59$ kPa .

3. Results

3.1. Dynamics of geometry change and growth potential distribution

In a single unconfined state *Methanosarcina* cells have a spherical shape with uniform cell wall growth and with μ_G distributed isotropically. Spatial confinement changes the internal stress state of a cell wall and hence the μ_G distribution which becomes anisotropic (Fig. 7-9). Cell wall growth becomes directed, governed by the growth potential. This growth anisotropy is the cell's response to the highly intensive stress state localized around a confinement region (Fig. 7-9, $t = 0$). Due to relaxation through directed growth, μ_G spatial variability decreases with time, and the cell follows more uniform and less intensive growth with decreased anisotropy (Fig. 7-9, $t = 0.3 - 1.0$). Nevertheless, the simulations clearly demonstrate the existence of principal directions of cell wall growth for spatially confined (aggregated) cells. Different and orthogonally oriented directions were found for all modelled representative conformations, consistent with experimentally observed observations (Fig. 10). Directions are pronounced at the initial stages of growth (Fig. 7-9, $t = 0.0 - 0.3$), where there are strong variations in μ_G distribution (and hence in directional growth) and tend to attenuate at the later stages.

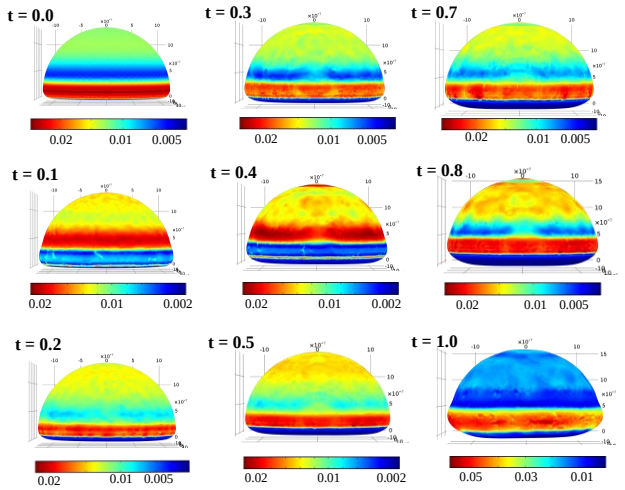

Fig. 7. Shape evolution and growth potential distribution for modeled conformation G1. The first stage of growth demonstrates intensive elongation in a direction orthogonal to the future expected division plane. This first stage is $\sim 1/3$ of predicted doubled-volume growing time (first 0.3 dimensionless time units). The second stage of growth (from 0.3 to 0.6 dimensionless time units) is characterized by intensive (multiple) switching of growth directions, however continues its intensive elongation during all this stage. During the third stage, diffusive-like type of growth was predicted, though anisotropy in

μ_G distribution was still preserved (time interval 0.6 – 1.0). The cell confinement results in directional growth localized at the regions which are close to confinement edge. This provides the cell wall stretching mostly at the mentioned regions in the direction parallel to plane of confinement ($t = 0 - 0.3$). At the later stages ($t = 0.6 - 1$) the growth is more diffusive (with increased isotropy of μ_G distribution due to smoothing its gradients during the previous time steps, $t = 0.3 - 0.6$) causes regression towards a hemisphere shape. Here, stages refer to different periods of growth within the representative conformation.

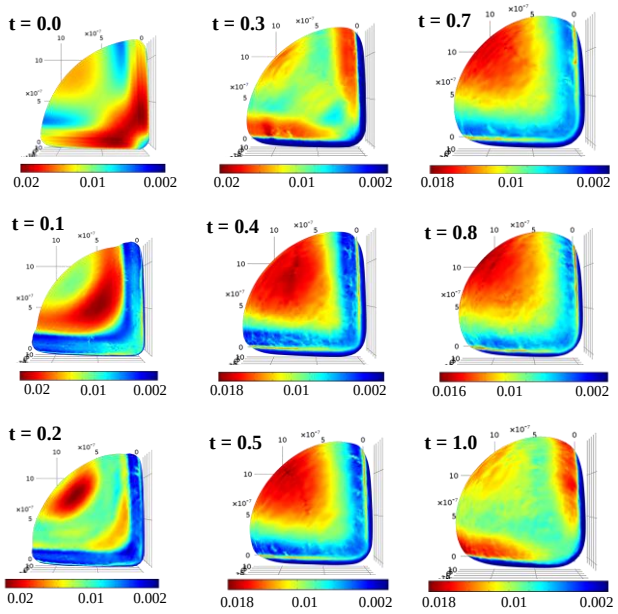

Fig. 8. Shape evolution and growth potential distribution for modeled conformation G2. The first stage of growth demonstrates intensive elongation in a direction orthogonal to the future expected division plane. This first stage is $\sim 1/3$ of predicted doubled-volume growing time (first 0.3 dimensionless time units). The second stage of growth (from 0.3 to 0.6 dimensionless time units) is characterized by intensive (multiple) switching of growth directions. The growth potential is more uniformly distributed at this stage. During the third stage, diffusive-like type of growth was observed, though anisotropy in μ_G distribution was still preserved (time interval 0.6 – 1.0). Here, stages refer to different periods of growth within the representative conformation.

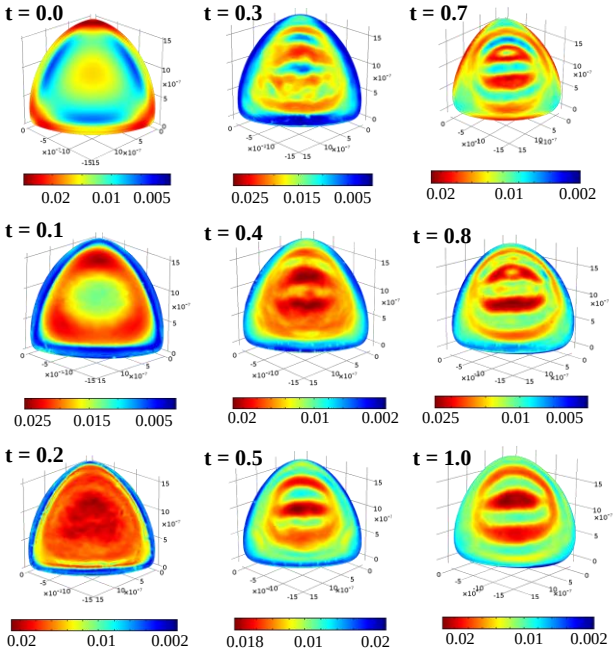

Fig. 9. Shape evolution and growth potential distribution for modeled conformation G3. The first stage of growth is characterized by directional growth in the plane parallel to future expected division plane (time interval 0.0 – 0.1). This stage is relatively short (0.1 dimensionless time units) and transfers to diffusive-like type of growth in the second stage with preserved anisotropy in μ_G distribution (time 0.2). The third, and the longest stage, shows focused directional growth in the axes orthogonal to future expected division plane (time interval 0.3 – 1.0). Here, stages refer to different periods of growth within the representative conformation.

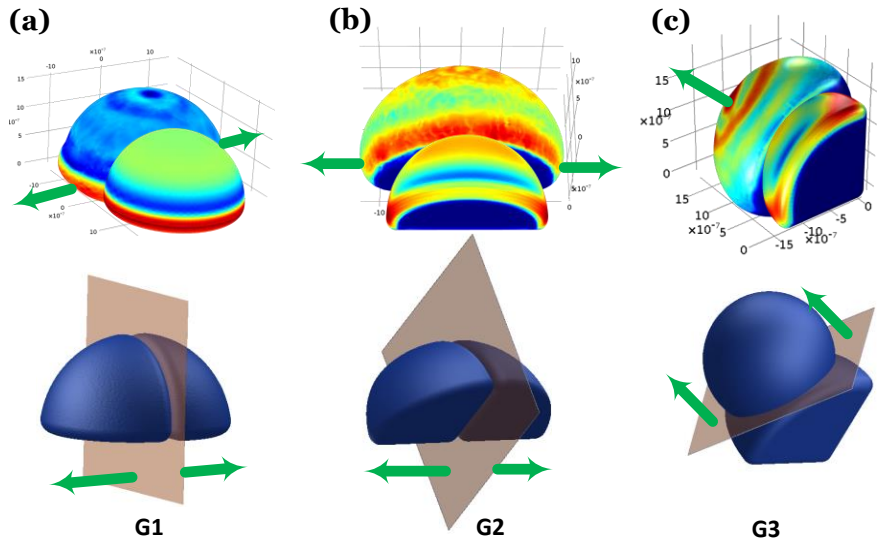

Fig. 10. Principal directions of growth. The top graphs show the

comparison of changes (caused by growth) in cells geometries at the initial moment of time ($t = 0$) and when the cells volume is doubled ($t = 1$). The green arrows indicate principal growth directions. The bottom graphs show the position of prospective division plane, predicted according to reported studies (see the Supplementary Materials for details), for each representative conformation. **(a)** The results of simulated growth for geometry G1; **(b)** for G2; and **(c)** for G3.

Neighboring cells within an aggregate are in close dynamic contact. Cell-cell interaction is simulated through the spatial confinement and defined on Ω_{conf}. The simulations demonstrate that due to the cohesive forces generated within Ω_{conf} (see Eq. 3), confined cells cannot deform substantially within their confined regions (reflecting observed results). This leads to substantially lower values of $\mu_G \in \Omega_{\text{conf}}$ observed for all modeled geometries during all periods. This also results in geometry conservation of confined regions with related (substantial) depletion of growth rates within Ω_{conf}. Moreover, $\mu_G \in \Omega_{\text{conf}}$ have isotropic spatial and temporal distributions (as discussed further below). The effect of confinement can be summarized as: i) due to μ_G gradients (determined by highly intensive stress state) localized around a confinement region, provide necessary conditions for intensive cell wall elongation at initial stages of growth (determining principal direction of growth, Fig. 10); and ii) confinement provides geometry conservation of neighboring cell-cell contact.

3.2. Anisotropy of growth potential distribution, and growth rate dynamics

The anisotropy in density distribution of μ_G absolute values is given in Fig. 11, (a)-(c). The anisotropy is calculated based on nonparametric kernel density estimation (KDE) of growth potential (Eq. 11) for each incremental time step. The map (Fig. 11, (a)-(c)) displays μ_G density distribution versus time and visualizes spatial and temporal cell wall growth intensity. The range of dominant μ_G values implicitly characterizes cells growth rate at the particular time interval.

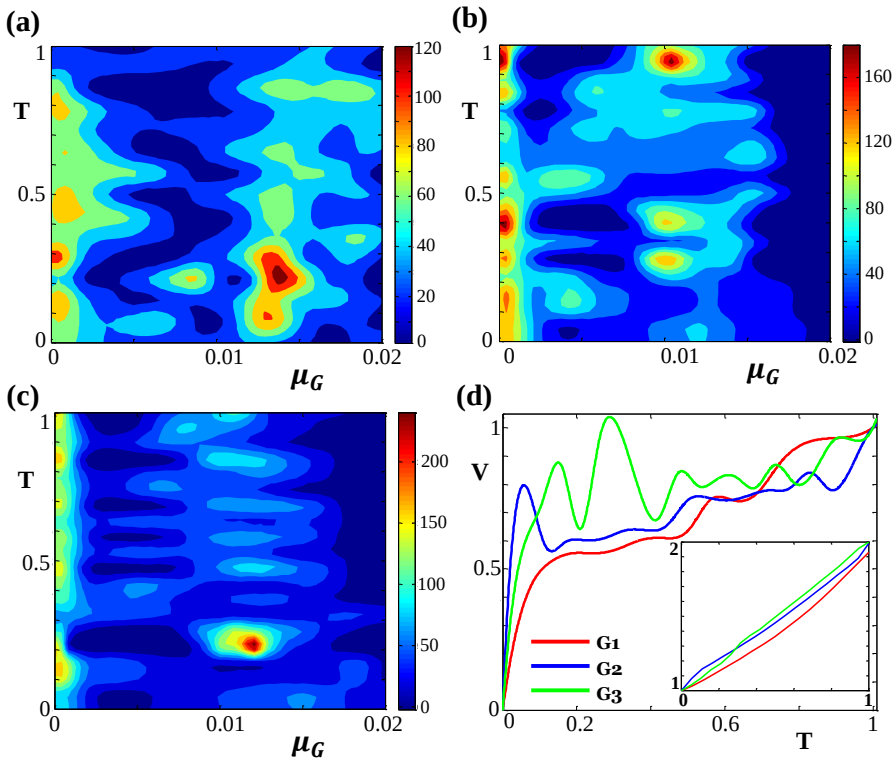

Fig. 11. Anisotropy map and a volume rate accumulation. Map of growth potential (μ_G) calculated based on kernel density estimation and displayed as a density distribution **vs** time (***T***). **(a)** Anisotropy map for conformation G1, **(b)** for conformation G2, and **(c)** for conformation G3. **(d)** Volume (***V***) rate accumulation (the main plot) and cumulative volume (inset plot) displayed for each modelled representative conformation.

The μ_G density distribution can be used as a measure of cell wall growth anisotropy. Pure isotropic growth has a uniform density distribution for a particular fixed time interval and any deviation from this kind of distribution indicates spatial anisotropy of growth intensity. Pure unconfined spherical cells have, and are directed by isotropic growth, while spatial anisotropic growth causes elongation.

In a similar way, anisotropy in time can be identified. Any variation in time from the initial μ_G density distribution (which does not need to be a uniform distribution) identifies dynamic growth anisotropy (growth rate anisotropy).

The anisotropy maps, which were constructed for each representative conformation (G1 - Fig. 11 (a), G2 - Fig. 11 (b), G2 - Fig. 11 (c)), show the variations in temporal and spatial μ_G density distribution for all modeled conformations which indicate significant growth anisotropy in spatially confined cells. Despite of observed anisotropy the character of temporal variations in spatial μ_G density distribution reveals the directional growth (which is generally preserved in time though is subject to variations) in all modeled geometries (Fig. S3).

The dynamic volume changes (main plot) and cumulative volume changes (inset plot), estimated for each modeled conformation, are shown in Fig. 11 (d). The main plot shows strong variations in cell volume changes during the first stages of growth, which tends to depletion in later stages. Despite of that, the cumulative growth rate (Fig. 11 (d), the inset plot) is close to linear. Since μ_G can be

evaluated as an indirect growth rate measure, dynamic cell volume profile can give the implicit estimation of μ_G anisotropy dynamics.

4. Discussion

4.1. Cell geometry sensing

The main contribution of the cell's confinement to the growth anisotropy is preservation within state variables the local geometry remaining from the previous division. This creates not only a local effect, where the new cell wall cannot be synthetized, but also a boundary condition to growing walls. This global (cell scale) effect appears as relaxation growth. This response leads to continuous change in local stress state affected by confinement, realized through growth anisotropy, such that the intense symmetric stretching in one particular direction can be observed.

Relaxation growth as cells respond to local geometry change is due to interaction of two coupled mechanisms - the mechanical and chemical responses, which constitute the main part of one whole cell's geometry sensing mechanism. The mechanical response is realized through the energy distribution according to the partition function φ_{mech}, Eq. (9, 10). This function φ_{mech} defines the amount of mechanical energy that is transformed to pure growth and amount of energy transformed to local structural changes of the cell wall. This energy transformation and its spatial distribution perform the main contribution to changes in dynamical physical properties of cell wall material (which are the chemical potential μ_{conf} and diffusivity D_{cw}). The μ_{conf} and D_{cw}, are key parameters which link mechanical and chemical parts of cell confinement detection.

The chemical response is realized by means of two following ways: diffusive transport of trisaccharide units GalNAc and GlcA through the cell wall material; and methanochondroitin synthesis inside the matrix layer. Movement of methanochondroitin building blocks (GalNAc, GlcA) as well as its assembly are driven by μ_{conf} under strong regulation by D_{cw}. Additional regulation is implemented through $\varphi_{\text{conf}}\boldsymbol{E_p}$, which is part of Eq. (10) which relates to a reduction of methanochondroitin assembly rate caused by increase in confinement free energy due to high polymerization intensity.

Here we suggest that cell sensing can be based on a simple passive regulation realized through chemical and thermodynamic response in cell wall potential to turgor pressure. This is enabled largely through implementation of the partition function, which distributes energy between polymer expansion and growth. Based these model results, changes in morphology can be realized without existence of any additional specialized active molecular machinery inside the cell and through basic conformational responses in growth. Though analysis cannot eliminate the possibility of active mechanisms, a passive, simple mechanism is more likely than an unnecessary specialized one.

4.2. Delayed growth of confined cells

Methanosarcina has a relatively low specific growth rate, which is $0.06h^{-1}$ for confined cells and $0.1h^{-1}$ for single unconfined cells [33]. Besides physiological and thermodynamic reasons, the specific growth rate in single unconfined cells is influenced by structural properties of the cell wall. The S-layer pore network, in which the average pore size $8-13\text{Å}$ is relatively narrow, such that

transport of GalNAc or GlcA is slow and this influences GalNAc, GlcA transport to polymerization sites. Another structural factor that can decrease cell wall growth rate is the thick methanochondroitin layer. It deforms under the turgor pressure load. In case of stretching deformation, this creates the room for trisaccharide polymerization. In the case of compression deformation, this reduces available volume for polymerization. Hence, methanochondroitin assembling cannot be realized within whole volume of methanochondroitin layer.

The next key question is why is the growth of confined cells significantly delayed compared to single (unconfined) cells? Besides structural and physiological factors discussed above, which has an impact regardless of confinement, two possible mechanisms related to confinement can be suggested based on model results. The first mechanism is restricted growth within the confined part of the cell wall. According to simulations, there is no growth within strongly confined regions, such that increased growth delay is expected with increasing confinement state. The second mechanism relates to the growth anisotropy. An aggregated cell, where cells are growing in confinement, can realize maximal possible growth rate per volume through diffusive growth only in the unconfined part of cell wall. This only exists for a small part of cell wall. Because of anisotropic distribution of growth potential, the maximum possible growth rate per volume can be realized only for a fraction cell wall, such that the average growth rate is much lower than in spherical unconfined cell.

The delayed growth as well as the directed growth of a cell wall are due to the spatial confinement of cells (in an aggregate). This confinement is formed by close contact between the neighboring cells and characterized by cell-cell interactions [45-47]. Similar contact interactions have been observed for cell-surface mechanical interactions, such as [27] where a cell–surface interaction was investigated theoretically by applying a two-dimensional mechanical model (interaction simulated using nonlinear springs). This concluded that a cell establishes focal adhesion sites with density dependent on the cell-wall stress. Mechanical cell-cell interactions have also been considered within biofilms [48-50]. For instance, in [50] the effect of cell properties on the structure of biofilms and microbial aggregates was investigated. This work identified that cell-cell interaction and adhesion, with adhesive links represented as springs, changed the colony morphology of rod-shaped cells (i.e., bacilli) through longitudinal growth/division stages. The key differentiation in the current paper identifies that the individual cell also responds to confinement, specifically directional and delayed growth for regularly aggregated cells (like in *Methanosarcina*). This means that not only the larger colony morphology (biofilm), but also the cell morphology is changed by intracellular interactions

4.3. Model results compared to observations. Consistency of directional growth and division plane orientation

The obtained morphological results are consistent with observations. The model is geometrically consistent with observations with finalized volume stretched along the axes as observed experimentally [2, 51, 52]. This gives an division plane position (according to experimental observations it placed orthogonally to the longest axes of the cell [53]) which is in fact the future confinement plane for daughter cells. The progression of representative conformations are consistent with observed aggregate evolution stage. That means, conformation G1 transforms to G2, which transforms to G3 (Fig. S2 a) (it could be seen if in place of predicted division plane put the developed septum which splits simulated grown cell to the two daughter cells which have the representative geometry configuration). This last geometry can either transform to weakly confined spherical cell - which constitutes the complete tetrad morphology; or transforms to a new conformation G1 - that constitutes the initiation of pseudoparenchyma morphology (Fig. 12).

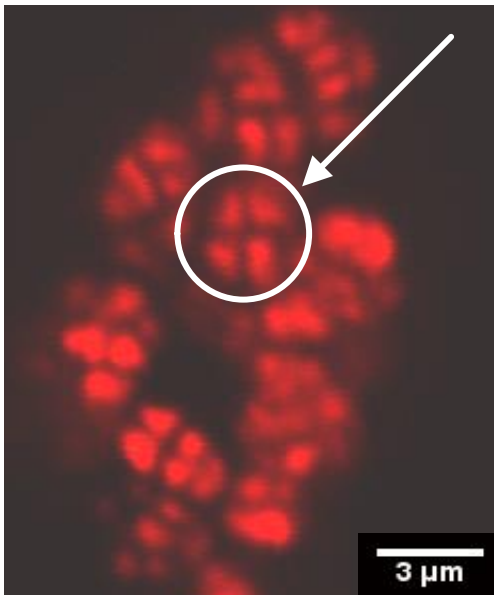

Fig. 12. Confocal microscope image of *Methanosarcina barkeri* aggregates. Culture grown on 20mM Acetate in carbonate free anaerobic media, originally sourced from DSMZ (www.**dsmz**.de). Culture was stained with 15mM 4',6-diamidino-2-phenylindole (DAPI) which binds to DNA and imaged on a Zeiss Axioscope LSM512 confocal microscope with 63x/1.40 Oil DIC objective. Methanochondroitin does not contain DNA and hence appears dark in the image. Arrow indicates cells in G3 conformation.

The second overall principle that supports the model's validity is its consistency with chromosome segregation time frame. It is known that the prokaryotic cell initiates DNA replication after achievement of specific cell length and split this process on different stages directly related to stages of cell elongation, the chromosome segregation starts after certain point of time when achieved specific critical cell length [54, 55]. Since the chromosome movement speed during segregation process is much higher than speed of cell growth [56], the cell should have enough space along the certain axes in order to support fast chromosomal movement in opposite directions. This means that the primary cell size increase is required to initiate the chromosome segregation. Chromosome segregation machinery is not independent and is associated with directional cell growth through the cytoskeleton based chromosome segregation system [56-61]. The nucleoid movement along the main axis does not depend on DNA synthesis, and the cell growth is more likely determined by the synthetic activity surrounding the nucleoid but not by the DNA amount in each chromosome [62]. So it is crucial to positioning the segregation machinery along the longest axes of the cell or more intensively stretching direction as soon as the cell starts to increase volume right after completing division. For all modeled geometries, simulation shows clear directional growth over a time span sufficient for longitudinal geometry needed correctly orient segregation machinery.

4.4. Application to confined bacterial cells

The theory presented here was specifically developed for archaeal cells. Archaeal specific features are mainly related to the polymeric methanochondroitin layer. However, because the model was derived based on work-energy principles it should be general enough to be easily extended to the case of bacterial cells. The key species specific variable in the model is chemical potential μ_{conf}. It, and the model in general, can be modified by taking into account the architecture of bacterial cell wall and properties of peptidoglycan network. The peptidoglycan network in Bacteria possesses similar properties as the methanochondroitin polymeric network in Archaea but with some differences. In particular, the peptidoglycan network demonstrates more rubber-like behavior and polymers network rearrangement can be completed if enzymatic activity is involved [63, 64]. This requires model extension to include mechanisms of enzymatic activity.

In general, regardless of modeled species, the partition function could be further developed, particularly based on possible experimental observations or species specific factors, since it is introduced in a simple form and can be improved further by considering dynamical polymerization activity of methanochondroitin.

5. Conclusions

This work develops a mathematical model for growth of confined prokaryotes, with a focus on Archaea, and particular application to *Methanosarcina*. As such, we derive the growth model within confined elastic shell approach that takes into account the detailed structure of archaeal cell wall, polymeric nature of methanochondroitin layer and is consistent with thermodynamics laws. In particular, a partition function is used to define the amount of energy that transformed to pure growth and to local structural changes of the cell wall material. The simple form of constitutive equation for the partition function was introduced. The developed model is applied to simulate 3D growth of archaeal cells for different representative conformations.

Simulations demonstrated strong growth anisotropy as well as changes in growth direction of cell wall due to confinement and shape evolution.

The theoretical framework indicates that cells may have a simple mechanistic sensing and response mechanism to confinement, with a passive regulation form, realized through a set of molecular processes effected during the cell's response to local geometrical changes without the need for specialized cellular mechanisms.

Acknowledgements

This research was financially supported by the Danish Strategic Research Council (Grant No. 10-093944). This project in Australia was supported by the ARC (project number DP0985000) and Dr. Damien Batstone is the recipient of an ARC Research Fellowship. We thank Natacha Juste-Poinapen from the University of Queensland for her assistance in providing and imaging the *Methanosarcina* culture.

References

1. M. M. Kendall and D. R. Boone, *The Order Methanosarcinales*, 2006.
2. R. W. Robinson, *Applied and Environmental Microbiology*, 1986, **52**, 17-27.
3. A. Zaritsky, C. L. Woldringh, I. Fishov, N. O. E. Vischer and M. Einav, *Microbiology-Uk*, 1999, **145**, 1015-1022.
4. E. Pas, M. Einav, C. L. Woldringh and A. Zaritsky, *Biochimie*, 2001, **83**, 121-124.
5. A. Pijper, C. G. Crocker and N. Savage, *Journal of bacteriology*, 1955, **69**, 151-158.
6. Canalepa.E, *Bacteriological Reviews*, 1970, **34**, 82-&.
7. T. Koyama, M. Yamada and M. Matsuhashi, *Journal of bacteriology*, 1977, **129**, 1518-1523.
8. M. Yamada, T. Koyama and M. Matsuhashi, *Journal of bacteriology*, 1977, **129**, 1513-1517.
9. R. D. Turner, E. C. Ratcliffe, R. Wheeler, R. Golestanian, J. K. Hobbs and S. J. Foster, *Nature Communications*, 2010, **1**.
10. H. Tzagoloff and R. Novick, *Journal of bacteriology*, 1977, **129**, 343-350.
11. W. B. Whitman, T. L. Bowen and D. R. Boone, *The Methanogenic Bacteria*, 2006.
12. Y. Liu and W. B. Whitman, in *Incredible Anaerobes: From Physiology to Genomics to Fuels*, ed. J. M. R. J. A. M. W. W. Wiegel, 2008, vol. 1125, pp. 171-189.
13. J. G. Ferry, *Methanogenesis : ecology, physiology, biochemistry & genetics*, Chapman & Hall, New York, NY [u.a.], 1993.
14. D. J. Batstone, C. Picioreanu and M. C. M. van Loosdrecht, *Water Research*, 2006, **40**, 3099-3108.
15. D. Karakashev, D. J. Batstone and I. Angelidaki, *Applied and Environmental Microbiology*, 2005, **71**, 331-338.
16. J. W. C. Dunlop, F. D. Fischer, E. Gamsjaeger and P. Fratzl, *Journal of the Mechanics and Physics of Solids*, 2010, **58**, 1073-1087.
17. M. Rumpler, A. Woesz, J. W. C. Dunlop, J. T. van Dongen and P. Fratzl, *Journal of the Royal Society Interface*, 2008, **5**, 1173-1180.
18. D. Loessner, J. A. Flegg, H. M. Byrne, J. A. Clements and D. W. Hutmacher, *Integrative Biology*, 2013, **5**, 597-605.
19. C. S. Chen, M. Mrksich, S. Huang, G. M. Whitesides and D. E. Ingber, *Science*, 1997, **276**, 1425-1428.
20. N. Minc, D. Burgess and F. Chang, *Cell*, 2011, **144**, 414-426.
21. N. Minc and M. Piel, *Trends in Cell Biology*, 2012, **22**, 193-200.
22. D. Ambrosi and F. Guana, *Mathematics and Mechanics of Solids*, 2007, **12**, 319-342.
23. D. Ambrosi and A. Guillou, *Continuum Mech. Thermodyn.*, 2007, **19**, 245-251.
24. A. Boudaoud, *Physical Review Letters*, 2003, **91**.
25. H. Jiang, F. Si, W. Margolin and S. X. Sun, *Biophysical Journal*, 2011, **101**, 327-335.
26. H. Jiang and S. X. Sun, *Soft Matter*, 2012, **8**, 7446-7451.
27. H. Jiang and B. Yang, *Journal of Biomechanics*, 2012, **45**, 209-217.
28. A. Goriely and M. Tabor, *Physical Review Letters*, 2003, **90**.
29. S.-V. Albers and B. H. Meyer, *Nature Reviews Microbiology*, 2011, **9**, 414-426.
30. A. Gambacorta, A. Gliozzi and M. Derosa, *World Journal of Microbiology & Biotechnology*, 1995, **11**, 115-131.
31. G. D. Sprott, C. J. Dicaire, C. G. Choquet, G. B. Patel and I. Ekiel, *Applied and Environmental Microbiology*, 1993, **59**, 912-914.
32. M. A. Arbing, S. Chan, A. Shin, T. Phan, C. J. Ahn, L. Rohlin and R. P. Gunsalus, *Proceedings of the National Academy of Sciences of the United States of America*, 2012, **109**, 11812-11817.
33. K. R. Sowers, J. E. Boone and R. P. Gunsalus, *Applied and Environmental Microbiology*, 1993, **59**, 3832-3839.
34. G. Seltmann and O. Holst, *The Bacterial Cell Wall*, Springer, 2002.
35. H. C. Aldrich, R. W. Robinson and D. S. Williams, *Systematic and Applied Microbiology*, 1986, **7**, 314-319.
36. B. M. Sattelle, J. Shakeri, I. S. Roberts and A. Almond, *Carbohydrate Research*, 2010, **345**, 291-302.
37. V. Vadillo-Rodriguez and J. R. Dutcher, *Soft Matter*, 2011, **7**, 4101-4110.
38. M. Ben Amar and A. Goriely, *Journal of the Mechanics and Physics of Solids*, 2005, **53**, 2284-2319.
39. S. M. Klisch and T. J. Van Dyke, *Mathematics and Mechanics of Solids*, 2001, **6**, 551-575.
40. A. Menzel and E. Kuhl, *Mechanics Research Communications*, 2012, **42**, 1-14.

41. H. Watanabe, *Progress in Polymer Science*, 1999, **24**, 1253-1403.
42. T. Bleha and P. Cifra, *Polymer*, 2003, **44**, 3745-3752.
43. E. K. Rodriguez, A. Hoger and A. D. McCulloch, *Journal of Biomechanics*, 1994, **27**, 455-467.
44. L. D. Landau, E. M. Lifshitz, A. M. Kosevitch and L. P. Pitaevskiĭ, *Theory of Elasticity*, Butterworth-Heinemann, 1986.
45. P. Giesbrecht, T. Kersten, H. Maidhof and J. Wecke, *Archives of Microbiology*, 1997, **167**, 239-250.
46. R. W. Robinson, H. C. Aldrich, S. F. Hurst and A. S. Bleiweis, *Applied and Environmental Microbiology*, 1985, **49**, 321-327.
47. P. Giesbrecht, T. Kersten, H. Maidhof and J. Wecke, *Microbiology and Molecular Biology Reviews*, 1998, **62**, 1371-+.
48. P. C. Y. Lau, J. R. Dutcher, T. J. Beveridge and J. S. Lam, *Biophysical Journal*, 2009, **96**, 2935-2948.
49. P. C. Y. Lau, T. Lindhout, T. J. Beveridge, J. R. Dutcher and J. S. Lam, *Journal of bacteriology*, 2009, **191**, 6618-6631.
50. T. Storck, C. Picioreanu, B. Virdis and Damien J. Batstone, *Biophysical Journal*, 2014, **106**, 2037-2048.
51. J. P. Touzel, D. Petroff and G. Albagnac, *Systematic and Applied Microbiology*, 1985, **6**, 66-71.
52. B. P. Lomans, R. Maas, R. Luderer, H. den Camp, A. Pol, C. van der Drift and G. D. Vogels, *Applied and Environmental Microbiology*, 1999, **65**, 3641-3650.
53. M. Almonacid and A. Paoletti, *Seminars in Cell & Developmental Biology*, 2010, **21**, 874-880.
54. W. D. Donachie and K. J. Begg, *Journal of bacteriology*, 1989, **171**, 4633-4639.
55. M. E. Sharpe and J. Errington, *Molecular Microbiology*, 1998, **28**, 981-990.
56. E. Toro and L. Shapiro, *Cold Spring Harbor Perspectives in Biology*, 2010, **2**.
57. J. Mierzejewska and G. Jagura-Burdzy, *Plasmid*, 2012, **67**, 1-14.
58. J. L. Ptacin, S. F. Lee, E. C. Garner, E. Toro, M. Eckart, L. R. Comolli, W. Moerner and L. Shapiro, *Nature Cell Biology*, 2010, **12**, 791-U746.
59. Z. Gital, N. A. Dye, A. Reisenauer, M. Wachi and L. Shapiro, *Cell*, 2005, **120**, 329-341.
60. C. L. Woldringh and N. Nanninga, *Journal of Structural Biology*, 2006, **156**, 273-283.
61. A. K. Kalliomaa-Sanford, F. A. Rodriguez-Castaneda, B. N. McLeod, V. Latorre-Rosello, J. H. Smith, J. Reimann, S. V. Albers and D. Barilla, *Proceedings of the National Academy of Sciences of the United States of America*, 2012, **109**, 3754-3759.
62. C. L. Woldringh, A. Zaritsky and N. B. Grover, *Journal of bacteriology*, 1994, **176**, 6030-6038.
63. W. Vollmer, D. Blanot and M. A. de Pedro, *Fems Microbiology Reviews*, 2008, **32**, 149-167.
64. W. Vollmer and S. J. Seligman, *Trends in Microbiology*, 2010, **18**, 59-66.

A mechanical mathematical model of cells has been developed to describe anisotropic growth of confined aggregated Methanosarcina. Response to external pressure, including orthogonal changes can be through simple mechanistic principles.

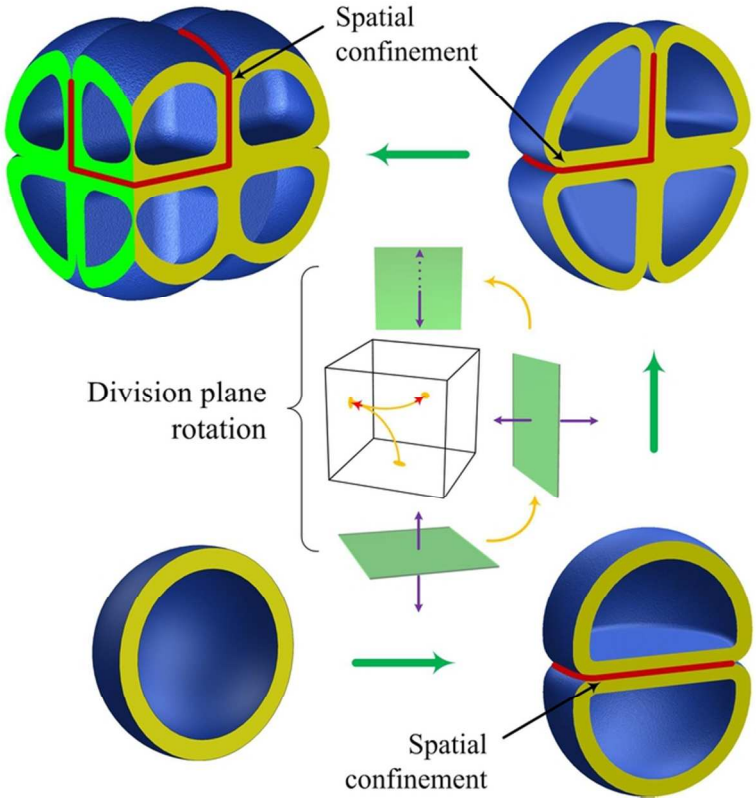

40x32mm (600 x 600 DPI)